Transition Metal—Carbon Bond Enthalpies as Descriptor for the Electrochemical Stability of Transition Metal Carbides in Electrocatalytic Applications

Journal of The Electrochemical Society, 2020 **167** 021501

Transition Metal—Carbon Bond Enthalpies as Descriptor for the Electrochemical Stability of Transition Metal Carbides in Electrocatalytic Applications

Daniel Göhl,[1,z] Holger Rueß,[2] Marc Pander,[1] Aleksandar R. Zeradjanin,[1,3] Karl J. J. Mayrhofer,[1,4,5,*] Jochen M. Schneider,[2] Andreas Erbe,[1,6] and Marc Ledendecker[1,z]

[1]*Department of Interface Chemistry and Surface Engineering, Max-Planck-Institut für Eisenforschung GmbH, 40237 Düsseldorf, Germany*
[2]*Materials Chemistry, RWTH Aachen University, 52074 Aachen, Germany*
[3]*Universität Bremen, Energiespeicher- und Energiewandlersysteme, 28359 Bremen, Germany*
[4]*Helmholtz-Institute Erlangen-Nürnberg for Renewable Energy (IEK-11), Forschungszentrum Jülich GmbH, 91058 Erlangen, Germany*
[5]*Department of Chemical and Biological Engineering, Friedrich-Alexander-Universität Erlangen-Nürnberg, 91058 Erlangen, Germany*
[6]*Department of Materials Science and Engineering, NTNU, Norwegian University of Science and Technology, 7491 Trondheim, Norway*

Transition metal carbides are used for various applications such as hard coating, heterogeneous catalysis, catalyst support material or coatings in fuel cell applications. However, little is known about the stability of their electrochemically active surface in aqueous electrolytes. Herein, the transition metal—carbon bond enthalpy is proposed as stability criterion for various transition metal carbides. The basis is an oxidation mechanism where the rate determining step is the metal—carbon bond cleavage under acidic conditions which was supported by a detailed corrosion study on hexagonal tungsten carbide. In situ flow cell measurements that were coupled to an inductively coupled plasma mass spectrometer corroborated experimentally the linear dependency of the oxidation overpotential on the transition metal—carbon bond enthalpy. The proposed model allows the estimation of the activation overpotential for electrochemical carbide oxidation resulting in a maximized stabilization for carbides in the 4th group (Ti, Zr, Hf). Together with the calculated thermodynamic oxidation potentials, TiC and VC exhibit the highest experimental oxidation potentials (0.85 V_{RHE}). The model can be used for preselecting possible carbide materials for various electrochemical reactions.
 [DOI: 10.1149/1945-7111/ab632c]

Manuscript submitted October 17, 2019; revised manuscript received December 5, 2019. Published January 9, 2020.

Supplementary material for this article is available online

List of symbols

H_{O-TM}	Transition metal—oxygen bond enthalpy
E_{Ox}	Apparent oxidation potential of a transition metal carbide
E_{TMC}	Thermodynamic oxidation potential of a transition metal carbide at experimental conditions
E^{o}_{TMC}	Thermodynamic standard oxidation potential of a transition metal carbide
$G^{\#}$	Chemical part of Gibbs free activation enthalpy
G_A	Total Gibbs free activation enthalpy
$G^{\#}_{C,A}$	Electrochemical (anodic and cathodic) part of Gibbs free activation enthalpy
j_{Ox}	Mininum current density where transition metal carbide oxidation is visible
j_o	Exchange current density
α_A, α_C	Anodic and cathodic symmetry factor
η_{Ox}	Activation overpotential for transition metal carbide oxidation
A	Pre-exponential factor
BVE	Butler-Volmer-equation
C	Bulk concentration of a reactant
H_{C-TM}	Transition metal—carbon bond enthalpy
F	Faraday's constant (96,485 C mol^{-1})
k	Reaction rate constant
n	Number of electrons transferred until the rate determining step
R	Ideal gas constant (8.314 J $(mol\ K)^{-1}$)
rds	Rate determining step
TMC	Transition metal carbide
σ, ε	Empirical parameters describing the dependence of activation enthalpy on bond enthalpies

The unique properties of transition metal carbides (TMC) such as metal-like electric conductivity, great hardness, high melting point, and chemical inertness, led to the usage of TMCs for various applications such as hard coatings for drilling and cutting tools, heterogeneous catalysis, catalyst support materials or coatings in fuel cell applications.[1–6] Despite their alluring properties and although their application as support or catalyst in electrocatalytic reactions has been explored intensively over the last years, the stabilities of TMCs have received only minor attention and general strategies for the (pre-) selection or evaluation of stable carbides are still wildly missing.[7–10] Often, the focus was laid on chosen materials for a particular application with little attempts to deduce general links to other carbide systems.[3,11–13] One exception is a study by Kimmel et al. which describes the galvanostatic oxidation of commonly used TMCs.[14] Oxidation potentials at various pH values were determined upon polarization at 0.1 mA cm^{-2} once the steady state was reached. However, the oxidation of the pristine surface might already take place at significantly lower potentials.[3,11] Catalytic reactions, either heterogeneous or electrochemical reactions, strongly depend on the solid/liquid interface and the nature of the surface. Material properties such as electrical conductivity or interfacial binding energies change drastically upon an evolution of a surface oxide monolayer.[15,16] However, the exploration of electrochemical properties of every TMC in its various stoichiometries and crystal structures requires time- and cost-intensive measurements. The here presented work sets out to establish a guideline for assessing the stability and corrosion behavior of refractory TMCs such as TiC, VC, NbC, TaC and WC in acidic media. Surface analysis tools like X-ray photoelectron spectroscopy (XPS) and In situ attenuated total reflection (ATR) FTIR spectroscopy are

*Electrochemical Society Member.
[z]E-mail: d.goehl@mpie.de; m.ledendecker@mpie.de

combined with In situ measurements on a flow cell, which was coupled to an inductively coupled plasma mass spectrometer (FC-ICP-MS), to provide a comprehensive model which allows for the estimation of the surface stability of early TMCs from commonly available thermodynamic data. Via interpolation, the model was expanded to various other TMCs which allows a preselection of possible TMCs for electrocatalytic applications.

Experimental

Transition metal carbide synthesis.—TiC, VC, NbC, TaC and WC thin films were deposited in a laboratory-scale sputtering chamber by direct current magnetron sputtering (DCMS). The base pressure was below 4×10^{-6} mbar and the Ar deposition pressure was 1 Pa. Polished single-crystalline Si (001) substrates (VC, NbC and TaC) or Al_2O_3 (001) substrates (WC, TiC) were arranged 10 cm away from the targets and heated to 700 °C during deposition. The transition metal target (TM = Ti, V, Nb, Ta, and W with power densities of Ti = 2.7 W cm^{-2}, V = 3.75 W cm^{-2}, Nb = 3.9 W cm^{-2}, Ta = 1.9 W cm^{-2}, and W = 2.3 W cm^{-2}) with an inclination angle of 45° with respect to the substrate normal and the C target (power density 9.9 W cm^{-2}) facing the substrate directly were sputtered between 66 to 90 min, resulting in film thicknesses between 500 and 800 nm, respectively. The chemical compositions of the as deposited thin films were determined by energy dispersive X-ray analysis (EDX) in a JEOL JSM-6480 scanning electron microscope (SEM) equipped with an EDAX Genesis 2000 system. X-ray diffraction (XRD) was used to study the structure using a Bruker AXS D8 Discover XRD equipped with a General Area Diffraction System (GADDS). The diffractometer was operated at a current of 40 mA and a voltage of 30 kV with Co Kα radiation at a fixed incident angle of 15°. For the VC sample, a GE Seifert X2-WS diffractometer was used at a current of 40 mA and a voltage of 30 kV with Co Kα radiation at a fixed incident angle of 2°.

X-ray photoelectron spectroscopy.—The surface composition of the transition metal carbide before electrochemical testing was determined on a Quantera II (Physical Electronics, *Chanhassen, MN, USA*), applying a monochromatic Al Kα X-ray source (1486.6 eV) operating at 15 kV and 25 W. The C1s signal at 284.5 eV was used to reference the binding energy scale. Analysis of the spectra has been carried out with CasaXPS. The oxide layer thickness d was calculated by

$$d = \lambda_O * \sin(\alpha) * \ln\left(\left(\frac{D_{TMC} * \lambda_{TMC}}{D_O * \lambda_O}\right) * \left(\frac{I_O}{I_{TMC}}\right) + 1\right) \quad [1]$$

where λ_O and λ_{TMC} are the inelastic mean free electron paths of the oxide and the transition metal carbide, D_{TMC} and D_O are the molar densities of the transition metal in the oxide and the carbide.[17–19] α is the angle between incident beam and analyzer, and I_O and I_{TMC} are the intensities of the oxide and the carbide in the sample.

Electrode pretreatment.—Before the measurements, native grown oxides were removed by treating WC, VC and NbC with an aqueous saturated NaOH solution, TiC with a 4:1 mixture of 0.5 M NaOH and 30% H_2O_2 and TaC with an ethanolic HF solution. Afterwards, the etching solution was removed with ultra-pure water (Elga PURELAB® Plus, 18 MΩ · cm, TOC < 3 ppb, Veolia Water Technologies, UK). XPS measurements confirmed the reduction of surface oxide coverage which was below one monolayer for all samples except NbC and TaC where ca. one monolayer of oxides was present (Fig. S6 is available online at stacks.iop.org/JES/167/021501/mmedia).[17–19] It is noted that other pretreatments such as less concentrated NaOH resulted in a higher surface oxide content of two to three monolayers for NbC and TaC.

Electrochemical flow-cell measurements.—The electrochemical measurements were conducted on a FC-ICP-MS (Schematic S1), which is described in detail elsewhere.[20] Sputtered transition metal carbide films on silicon substrates or commercial hexagonal tungsten carbide (WC_{hex}) particles (d_p = 190 nm, *Sigma-Aldrich*, USA) deposited on a glassy carbon plate (loading 1.3 μg spot^{-1}) were used as working electrode (WE). The electrical contact to the WE was ensured via a small steel needle. The geometric electrode area was determined by the opening of the FC to be 0.011 cm^2. The real electrode surface area was assumed to be identical for the sputtered films and a roughness factor of one was assumed. For WC_{hex}, the geometrically calculated surface area was used. All currents and dissolution rates were normalized to the surface area. A commercial Ag/AgCl (3 M KCl, *Metrohm AG, Switzerland*) electrode, placed after the outlet of the FC, served as reference electrode (RE). Prior to each measurement, the potential vs RHE was determined by means of a polished Pt foil to be at +0.264 V (±1 mV). All potentials herein are stated vs RHE. The counter electrode (CE) was a graphite rod placed before the inlet. A 0.1 M $HClO_4$ solution was used as electrolyte which was prepared by mixing concentrated perchloric acid (*Merck, Germany*, Suprapur®, 70%) with ultrapure water. The electrolyte was stored in a small reservoir that can be purged with different gases. From this reservoir, it was pumped with a peristaltic ICP-MS pump at constant flow rate of 188 μL min^{-1} through the FC. For all measurements, the electrolyte was purged with Ar. After the electrolyte left the FC, it was mixed via a V-connector with an internal standard solution containing 10 μg l^{-1} of Re, Sc and Y. Afterwards, the electrolyte was introduced to the ICP-MS (*NexION 350X, Perkin Elmer, USA*). The ^{45}Sc, ^{48}Ti, ^{50}V, ^{89}Y, ^{93}Nb, ^{181}Ta, ^{184}W and ^{187}Re isotopes were measured to monitor the concentration in the electrolyte.

To establish a detailed correlation between applied potential and oxidation current/dissolution, a cyclic voltammogram (CV) was conducted with a scan rate of 3 mV s^{-1} from −0.2 V to +1.5 V_{RHE}. In case of VC, the upper vertex potential was reduced to 1.15 V_{RHE} because of extensive corrosion. The delay time between onset of dissolution at the working electrode and detection at the ICP-MS detector was 17 s, which was compensated by calibrating the time scale. The peak dissolution has, however, a further uncompensated delay of 10–15 s because of the plug-flow-type concentration profile. Therefore, the resolution of the potential determinations is 30–-45 mV at a scan rate of 3 mV s^{-1}. The oxidation potential was determined as the potential where the current was higher than three times the standard deviation of current in the double layer charging region.

To determine the oxide surface coverage of hexagonal WC particles before the oxidation potential as determined in the experiment described in the previous paragraph, the particles were polarized for 5 min at 0.45 V_{RHE}.

In situ electrochemical ATR-FTIR spectroscopy.—For In situ FTIR measurements, a commercial ATR-FTIR spectrometer was modified as displayed in Schematic S2. A freshly cleaned silicon single-crystal (⟨100⟩; N-doped 1–30 ohm cm; Floating zone growth; 52 mmm × 20 mm × 2 mm in size, 30° angles on the small sides of the base) was coated with 1 ml of an aqueous suspension of WC particles (47 mg l^{-1}) via drop casting. For the electrochemical potential control, a potentiostat (IviumStat XR, *Ivium Technologies, the Netherlands*) was used in a home-made three electrode setup. The freshly coated silicon crystal served as WE, and the CE was a Pt-sheet with a surface area of 0.025 cm^2. A commercial Ag/AgCl electrode (3 M KCl, *Metrohm*) served as RE with a potential of +270 mV vs RHE. To conduct spectroscopic measurements, the electrochemical setup was placed in the beam path of an FTIR spectrometer (FTS 30 00 MX Excalibur Series, *Bio-Rad Laboratories Inc., USA*) to achieve an internal reflection setup. The silicon crystal worked as internal reflection element. Chronoamperometric measurements were conducted every 100 mV in a potential range from −0.13 to 1.27 V_{RHE} in 0.1 M $HClO_4$. At each potential, 8192 FTIR scans were recorded without a polarizer resulting in a measurement duration of about 30 min per step. Prior to the spectroscopic measurement, 20 cyclic voltammetry cycles

were conducted in the range of −0.33 to 0.47 V_{RHE} at a scan rate of 200 mV s^{-1} as cleaning procedure. Difference absorbance spectra were calculated initially for both experiments with respect to the initial potential of −0.13 V_{RHE}. In order to extract the WC contributions, a background experiment with the same method was conducted on an uncoated Si-ATR crystal. The difference absorbance of pure Si was multiplied with a factor and subtracted from the absorbance of WC at the corresponding potential. The subtraction factor was chosen to cancel the peak visible at 1040 cm^{-1} in the Si spectra, in a similar fashion as common practice for the subtraction of residual water vapor contributions (For further information see supplementary information (SI) and Fig. S1).[21]

Results

Oxidation overpotential of hexagonal tungsten carbide.—The coupling of the electrochemical FC to the ICP-MS allows for the simultaneous detection of electrochemical processes such as oxidation (changes of oxidation states) and dissolution processes.[20,22] Therefore, it is possible to distinguish between those two elementary steps, and hereinafter, the following terminology is used: oxidation refers only to the detection of an anodic current (electrochemical oxidation, irrespective of dissolution or passivation) while dissolution refers only to the detection of a concentration increase in the electrolyte. In an early study, we evaluated the electrochemical stability of WC_{hex} particles in 0.1 M $HClO_4$ between 0.0 and 1.5 V_{RHE} with the FC-ICP-MS.[23] In that study, WC_{hex} was chosen as it is one of the most discussed TMCs for electrocatalytic applications.[9,24–27] The results demonstrated an enhanced stability of WC_{hex} in contrast to metallic W. According to the reaction equation,

$$WC + 4H_2O \rightarrow WO_2 + CO_2 + 4H_2 \quad [2]$$

the thermodynamic stability increase is only minor with an enthalpy of formation of $\Delta H^f = -38$ kJ mol^{-1} corresponding to a thermodynamic oxidation potential of 0.03 V_{RHE} (detailed information on oxidation potential calculations can be found in the SI).[6,11,12,28–36] However, in contrast to W, which oxidizes and dissolves already at 0.0 V_{RHE}, WC oxidation occurs above 0.6 V_{RHE}. Thus, the kinetic overpotential (η, difference between thermodynamic and observed oxidation potential) for WC_{hex} oxidation is 570 mV.[23]

In earlier literature reports, this was attributed to surface passivation of WC. This would imply a preceding oxidation process; however, in our study we did not observe any preceding oxidation current. To elucidate more on the oxidation mechanism of WC_{hex} particles, In situ electrochemical FTIR measurements on a silicon internal reflection element were conducted. While the WC_{hex}/Si ATR crystal was polarized at various potentials ranging from −0.13 to 1.27 V_{RHE}, FTIR spectra were recorded in situ. As the supporting Si ATR—crystal exhibits absorbance bands in the same wavenumber region, background spectra were recorded at the same potentials and subtracted from the WC spectra to differentiate effects from the Si/$HClO_4$ interface.

At 1,040 and 1,220 cm^{-1}, two broad vibrational bands were observed in the raw spectra (Fig. S2). The subtraction of the peak at 1,040 cm^{-1} can serve as a quality criterion for the subtraction of the features originating only from Si. Figure 1 shows the respective subtraction spectra between 950 and 1,400 cm^{-1} referenced to the spectrum at -0.13 V_{RHE}. At potentials below 0.67 V_{RHE}, the subtractions leave residual negative difference absorbance in the order of 10^{-4} in a dispersive peak with a maximum at ∼1,290 and minimum at ∼1,330 cm^{-1}. Due to the low absorbance, a systematic interpretation of this specific feature is highly challenging. Small positive difference absorbances are observed in the broad peak at 1,100 cm^{-1}, indicating likely a small increase in the SiO_2 layer thickness on the surface. When the potential 0.67 V_{RHE} is exceeded, a clear negative difference absorbance at ∼1,220 with a shoulder around ∼1,250 cm^{-1} becomes visible. These features become more and more pronounced with increasing potential, and reach absorbance levels of several 10^{-3} (Fig. 2). A broad peak at 1,220 cm^{-1} has been reported for WC_{hex} which agrees with the peak position observed here.[37] The observed negative difference absorbance starting at the apparent oxidation potential of 0.6 to 0.7 V_{RHE} is thus consistent with the oxidative dissolution of WC. Based on the absorbance trajectory and FC results from our first study,[23] a mechanism of adsorption and oxidation is proposed as illustrated in Fig. 2. Below the apparent oxidation potential of WC, water molecules adsorb onto the WC surface at low potentials, partially oxidizing the outer surface layer chemically. As only the outer surface is affected, the WC absorbance does not decline and electrochemical redox reactions do not take place as no current flow is detected in this regime.[23] At potentials above 0.6 V_{RHE}, WC is oxidized, leading to a decline in WC absorbance as the surface becomes covered with tungsten oxides and hydroxides.[11,38] According to FC-ICP-MS results,[23] 1 monolayer is dissolved up to 1.1 V_{RHE} resulting in a decrease in relative absorbance of 0.002

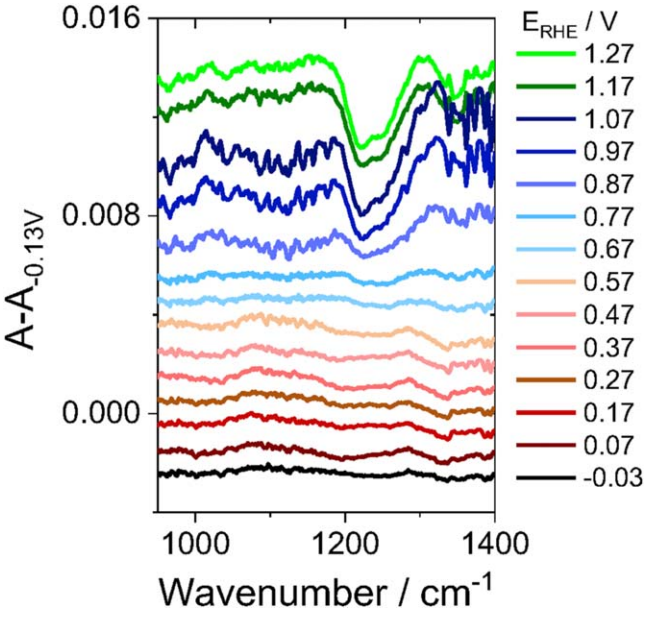

Figure 1. FTIR absorbance (A) spectra of hexagonal WC particles on a Si-ATR-crystal at potentials from −0.03 to 1.27 V_{RHE} in 0.1 M $HClO_4$. The spectra were referenced to a spectrum at −0.13 V_{RHE}, and Si background spectra were subtracted.

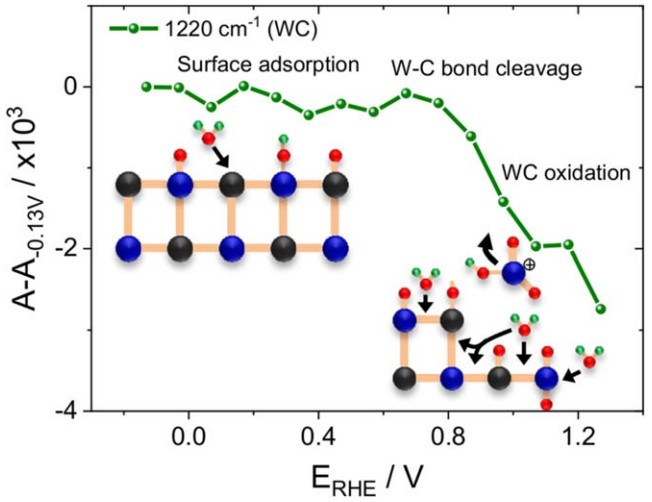

Figure 2. Absorbance difference development of W-C vibrational modes from −0.13 to 1.27 V_{RHE} and schematics of the oxidation mechanism. Black sphere = C, blue = W, red = O, green = H.

between 0.6 and 1.1 V_{RHE}. As the absorbance decline in the adsorption/chemical reaction regime is a factor of ten smaller, less than a monolayer of the surface has been partially oxidized before the onset of electrochemical oxidation corroborating the proposed mechanism. This is supported by an additional FC experiment in which WC_{hex} particles are polarized 5 min at 0.45 V_{RHE}, which is 100–150 mV below the apparent oxidation potential. The W dissolution profile revealed negligible dissolution and XPS measurements prior to and after the experiment revealed an oxide coverage of 0.3 monolayers (Fig. S3). This indicates neither that oxidation occurs nor that a passivation layer forms below 0.6 V_{RHE}. Hence, W-C bond rupture does not occur.

The dependency of the oxidation overpotential on the TM-C bond enthalpy.—To obtain a more extensive overview of the stabilization of various TMCs and to corroborate that the transition metal—carbon (TM—C) bond rupture is the rate determining step (rds) in the TMC oxidation, the electrochemical behavior of several sodium chloride isomorph transition metal carbides (TiC, VC, NbC, TaC and face centered cubic tungsten carbide (WC_{fcc})) was investigated. Various TMC thin films (500 nm) were prepared via magnetron sputtering, and the carbide phase formation and stoichiometry was controlled via XRD, SEM-EDX, and XPS (Figs. S4 to S6, Table SI).[39] Native grown oxides were removed chemically prior to electrochemical measurements (Fig. S6), which consisted of a CV between −0.2 and 1.5 V_{RHE} at 3 mV s^{-1} in Ar-sat. 0.1 M $HClO_4$ on the FC-ICP-MS (Figs. 3a–3e). An exception was VC where the upper potential limit was restrained to 1.15 V_{RHE} because of excessive corrosion (Fig. 3b). Of the five investigated TMCs, TiC and TaC show the expected electrochemical behavior for strongly passivating materials with an oxidation peak followed by a passive region with reduced oxidation current. VC shows a non-passivating behavior with a steadily increasing oxidation current at higher potentials. The CVs of NbC and WC_{fcc} are in between these two cases. Instead of a clear oxidation peak, a plateau is observed 100–200 mV after the beginning of oxidation. For WC_{fcc}, a sudden current increase starting from 1.2–1.3 V_{RHE} indicates the trans-passivation regime, whereas for NbC, the current density only slightly increases starting from 1.2 V_{RHE}. The differences in current response are mirrored in the distinct dissolution profiles (Figs. 3a–3e). As VC does not passivate, the oxidative dissolution concentration increases steadily until the scan direction is reversed. We note that the peak dissolution is delayed by about 100 mV due to the plug flow type profile of the electrolyte in the tubing. For the strongly passivating carbides TiC and TaC, a dissolution peak with a delay of 100 mV to the oxidation current peak is observed. Afterwards, the dissolution decreases indicating the formation of a passivation layer as the solubility product of oxidized metal cations is exceeded near the surface.[11] The Nb dissolution shows the same trend with a peak dissolution around 1.1 V_{RHE} leading to the conclusion that the observed oxidation current at potentials above 1.1 V_{RHE} does not lead to dissolution but to a steadily growing oxide overlayer. For WC_{fcc} during the anodic scan, the dissolution profile is analogous to the CV with an oxidation plateau above 0.55 V_{RHE} (magnified CV and dissolution profile in Fig. S7) and a strong rise in W-concentration in the trans-passivation regime above 1.2–1.3 V_{RHE}. However, when the scan direction is reversed at the vertex potential of 1.5 V_{RHE}, the dissolution concentration does not decrease again from the high level reached during trans-passivation until the oxidation potential at 0.55 V_{RHE} is reached. The electrochemical behavior of the sputtered WC_{fcc} is slightly different than for WC_{hex} particles.[23] The oxidation of WC_{hex} is delayed for about 50mV towards higher potentials. WC_{hex} begins to passivate above 1.2 V_{RHE} in comparison to 0.9 V_{RHE} for WC_{fcc} and trans-passivation does not occur for WC_{hex} in the investigated potential window. These observations might be related to the higher thermodynamic stability and also higher W—C bond enthalpy of WC_{hex} as discussed in the course of the manuscript.[40]

The CVs and the dissolution profiles of all synthesized TMCs can be divided into three main regions: 1) the adsorption/chemical reaction region below the oxidation potential, 2) the surface oxidation regime, and 3) the passivation region. Deviations from this behavior are the missing passivation region for VC, and an additional trans-passivation region for WC_{fcc} above 1.3 V_{RHE}. A more detailed discussion of the passivation behavior and dissolution profiles can be found in the SI and Fig. S8. For the discussion of the oxidation mechanism, only onset potentials for the carbide oxidation (E_{ox}^{exp}) will be determined. Here, the point of E_{ox}^{exp} is determined as three times the noise or standard deviation of the baseline of both the CV and the dissolution profile. The determined values are summarized in Fig. 3f for the investigated TMCs. According to Cowling and Hintermann, TiC is stepwise oxidized with the formation of intermediate lower valent oxides and CO_2.[11,12] If similar reaction pathways are considered for all TMCs, the thermodynamic standard oxidation potentials (E_{TMC}^{o}) can be calculated from reaction Eqs. S7 to S18 according to Eq. S6 (Table I and SII). The thermodynamic oxidation potentials at experimental conditions (E_{TMC}) can be calculated according to the Nernst equation as

$$E_{TMC} = E_{TMC}^{o} + \frac{RT}{zF} * \ln\left(p(CO_2)^{y} * p(H_2)^{x}\right) = E_{TMC}^{o} + \frac{RT}{zF} * \ln\left(p(CO_2)^{y}\right) \quad [3]$$

considering an electrolyte concentration of 0.1 M $HClO_4$ and assuming a CO_2 partial pressure of 10^{-6} bar (values summarized in Fig. 3f and Table I).[29,30] A comparison between thermodynamically calculated E_{TMC} and experimentally observed E_{ox}^{exp} reveals large differences between these two quantities and thus, large oxidation overpotentials (η) ranging from 520 mV for WC_{fcc} to 940 mV for TiC (Fig. 3f). If the overpotential is correlated to the TM—C bond enthalpy ($H_{C\text{-}TM}$, values obtained previously[41] and summarized in Table SIII), a linear dependency is observed (Fig. 4). This suggests that the rupture of the TM—C bond is the rds of the TMC oxidation. In this respect, the largest overpotential is observed for TiC which has the highest $H_{C\text{-}TM}$ of the investigated TMCs.[41] The reason for that will be discussed later.

Discussion

Correlation of bond enthalpy and overpotential.—So far, the results suggest that the TM—C bond plays a critical role in the stabilization of TMCs. The comparison between WC_{hex} and metallic

Table I. Calculated thermodynamic standard (E_{TMC}^{o}) and experimental oxidation potentials of transition metal carbides (E_{TMC}) from the 3rd to the 6th group according to Eqs. S6 and 3, the reaction Eqs. S7 to S18 and the Gibb's free formation enthalpies and standard entropies of the reactants and products (Table SII).

	E_{TMC}^{o} /V_{SHE}	E_{TMC} /V_{RHE}		E_{TMC}^{o} /V_{SHE}	E_{TMC} /V_{RHE}
Sc_2C	−1.01	−1.05	VC	0.02	−0.04
Y_2C	−1.03	−1.07	NbC	0.10	0.04
La_2C	−0.90	−0.94	TaC	−0.16	−0.20
TiC	−0.03	−0.09	Cr_3C_2	−0.16	−0.20
ZrC	−0.37	−0.41	Mo_2C	0.01	−0.02
HfC	−0.36	−0.40	WC	0.07	0.03

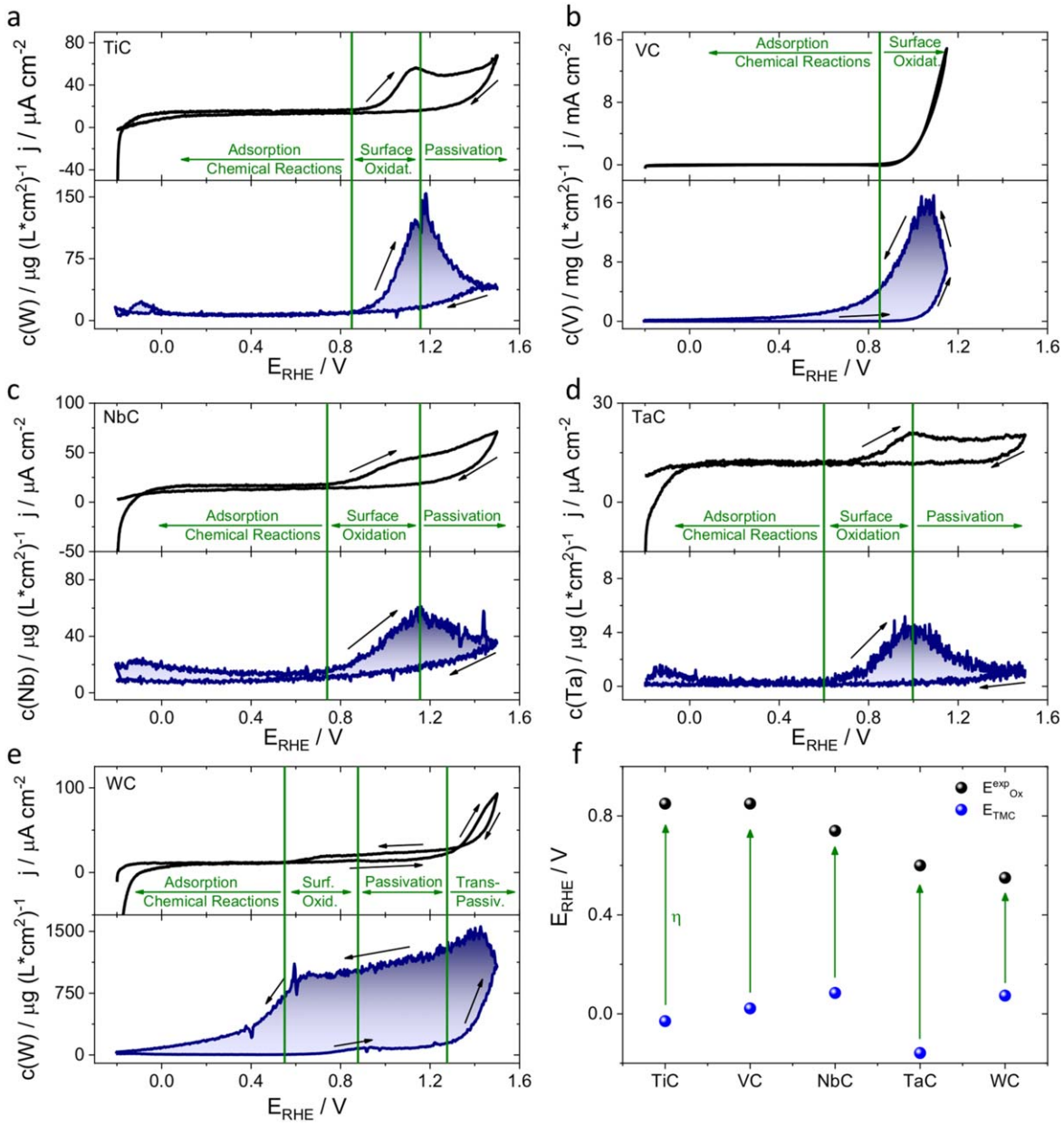

Figure 3. Cyclic voltammograms of (a) TiC, (b) VC, (c) NbC, (d) TaC and (e) WC from −0.2 to 1.5 V_{RHE} at a scan rate of 3 mV s^{-1} in Ar-sat. 0.1 M $HClO_4$ together with the corresponding dissolution concentration profiles. (f) Thermodynamic reversible oxidation potentials E_{TMC} calculated according to Eq. 3, and the observed oxidation potentials E_{ox}^{exp} for the investigated thin film transition metal carbides.

W showed an increase in oxidation potential of 600 mV.[23] As the thermodynamic stabilization was calculated to be only 30 mV, an overpotential of 570 mV was observed for the oxidation reaction indicating that the stabilization of the TMCs is caused by kinetic stabilization.[23] As the solubility of oxide reaction products is the same for metals and carbides, it is hypothesized that the kinetics are slowed down by the TM—C bond formation. According to molecular orbital theory, the bonding in TMCs is mainly based on the hybridization of the metal's d-band with the carbon's p-band.[1,41] On an atomic scale, the three t_{2g} metal orbitals can overlap with the three p orbitals of carbon creating each a σ and two π bonding and antibonding orbitals. The remaining two e_g metal orbitals do not overlap with carbon orbitals and stay mainly metallic. As calculated by Häglund et al., the occupancy of the bands is the crucial factor describing both the structure and thermodynamic stability of the TMCs.[41] The four bonding bands can be occupied by 8 valence electrons, and at this configuration, the Fermi level lies in a minimum between bonding and antibonding orbitals. Therefore, a maximum formation enthalpy and bonding enthalpy is observed for the 4th group with TiC, ZrC and HfC.[41,42] If the number of electrons is further increased, nonbonding, mostly metallic δ-bands or antibonding pd-bands have to be filled. The enthalpy of formation continuously decreases and carbides become less stable when approaching the late transition metals.[41,43] Following that, a high overpotential for the electrochemical carbide oxidation is needed for the rupture of the metal—carbon bond. The electrochemical reaction rate in dependence of the overpotential can be expressed by the Butler-Volmer-equation (BVE),

$$j = j_0 * \left(\exp\left(-\frac{\alpha n F \eta}{RT}\right) - \exp\left(\frac{(1-\alpha) n F \eta}{RT}\right)\right) \quad [4]$$

whereas the exchange current density j_0 is a measure for the intrinsic reaction rate, n is the number of electrons transferred in the rate determining step, η is the overpotential (difference between applied and reversible potential), F is the Faraday constant (96,485 C mol^{-1}),

R is the ideal gas constant (8.314 J (mol K)$^{-1}$), T is the temperature and α is the symmetry factor.[44,45] The BVE describes the dependency of the current on the applied overpotential in case of outer sphere charge transfer reactions without mass transport. In our case, an inner sphere charge transfer takes place, but in case that the bond cleavage (charge transfer) is the rds, the BVE can be also applied.[46] Mass transport of water molecules can be neglected in aqueous media for the oxidation of the outermost carbide layer. The BVE can not be applied if a passivating oxide layer is present on the surface. However, XPS and FTIR experiments revealed that less than a monolayer is present on the carbide surface before the apparent oxidation potential is reached (Figs. 2, S6 and S3). Therefore, the BVE can be used to describe the current-potential dependency around the observed oxidation potentials E_{Ox} where passivation has not occurred yet (Fig. S8). As the carbide oxidation is an irreversible reaction and the overpotentials are large, the cathodic component of the BVE can be neglected and the BVE simplifies to the Tafel Eq. 5.[47]

$$j = j_o * \exp\left(\frac{\alpha_A nF\eta}{RT}\right) \quad [5]$$

Usually, j_o represents the reaction rate of the dynamic equilibrium and displays the net flux of ions reacting at the electrode,

$$j_o = nFkC \quad [6]$$

which is given by current per ion (nF), the reaction rate constant (k) and the bulk concentration (C).[44] For an irreversible reaction, an equilibrium does not exist and the determined j_o value is only valid in the examined potential window.[47] A reaction rate constant k of a half reaction is given by the Arrhenius equation

$$k = A * \exp\left(-\frac{G_A}{RT}\right) = A * \exp\left(-\frac{(G^{\#} + G^{\#}_{EC}}{RT}\right) \quad [7]$$

where A is the pre-exponential factor and G_A is the Gibbs free activation enthalpy. G_A can be split into a chemical $G^{\#}$ and electrochemical ($G^{\#}_{EC}$) part.[44] As $G^{\#}$ is the crucial parameter for the intrinsic activation overpotential, Eq. 7 simplifies to

$$k = A * \exp\left(-\frac{G^{\#}}{RT}\right) \quad [8]$$

In case of a three body system C, O, TM in which the reaction

$$C - TM + O \rightarrow C + TM - O \quad [9]$$

takes place, the bond enthalpies of C-TM ($H_{C\text{-}TM}$) and O-TM ($H_{O\text{-}TM}$) can be used to estimate $G^{\#}$ according to the method of Kagiya et al.[48] displayed in

$$G^{\#} = H_{C-TM} * (1 - \sigma E_{O-TM}) - \varepsilon H_{O-TM} \quad [10]$$

where σ and ε are empirical parameters and differ upon the class of reaction such as nucleophilic substitution or radical reaction.[48–50] The method's error in the estimation of $G^{\#}$ is about 8 kJ mol^{-1}.[48] The insertion of Eqs. 10 and 8 into Eq. 6 yields

$$j_o = nFCA * \exp\left(-\frac{H_{C-TM} * (1 - \sigma H_{O-TM}) - \varepsilon H_{O-TM}}{RT}\right) \quad [11]$$

which expresses the exchange current density in dependency of the reactant and product bond enthalpies. Combination of Eq. 11 with the anodic part of the BVE (Eq. 5) results in

$$j = K * \exp\left(-\frac{H_{C-TM} * (1 - \sigma H_{O-TM}) - \varepsilon H_{O-TM}}{RT}\right) * \exp\left(\frac{\alpha_A nF\eta}{RT}\right) \quad [12]$$

which is a description of the observed current density in dependency of overpotential η and the bond enthalpies. The point, where a clear oxidative current j_{Ox} is detected, may now be determined as the apparent oxidation potential E_{Ox}, and Eq. 12 can be solved for the required minimum overpotential η_{Ox}

$$j_{Ox} = K * \exp\left(-\frac{H_{C-TM} * (1 - \sigma H_{O-TM}) - \varepsilon H_{O-TM}}{RT}\right) * \exp\left(\frac{\alpha_A nF\eta_{Ox}}{RT}\right)$$

$$\ln\left(\frac{j_{Ox}}{K}\right) * RT = D_{Ox} = -H_{C-TM} * (1 - \sigma H_{O-TM}) + \varepsilon H_{O-TM} + \alpha_A nF\eta_{Ox}$$

$$H_{C-TM} * \frac{(1 - \sigma H_{O-TM})}{\alpha_A nF} - \frac{\varepsilon}{\alpha_A nF} H_{O-TM} + D^*_{Ox} = \eta_{Ox} \quad [13]$$

According to Eq. 13, the higher the TM–O bond dissociation, the smaller is the term $\frac{(1 - \sigma H_{O-TM})}{\alpha_A nF}$. Therefore, $G^{\#}$ and η_{Ox} decrease with rising H_{O-TM}. If H_{O-TM} becomes increasingly large, the first part of Eq. 13 can be neglected and Eq. 13 becomes a function of the second part $\frac{\varepsilon}{\alpha_A nF} H_{O-TM}$. In that case, η_{Ox} is linearly dependent on the oxide bond strength. This correlation was observed by Kimmel et al. for refractory carbides in alkaline media, while it was not observed in acidic electrolytes.[14] The reason behind might lie in the electronic structure of the surface of early TMCs, which was reported to be similar to noble metals,[1,4] and hence, adsorption of electron donating molecules such as oxygen is expected to be less likely.[7,51] Yet, the covalent character of the TM-C bond and the difference in electronegativity create a polar surface leading to an electron density transfer from the metal sites to the neighboring carbon sites. This leads to a positive partial charge at the metal center which was corroborated by near edge X-ray absorption fine structure experiments.[52] As a consequence, the metal is susceptible to nucleophilic attacks. The concentration of nucleophilic hydroxide anions is high in alkaline media which eases the formation of TM–OH bonds, and facilitates TM–C bond cleavage. Density functional theory (DFT) calculations by Michaelidis et al. showed that OH-adsorption energies are in the range of the TM—C bond energy explaining the observation made by Kimmel et al.[53] Hydroxide anions are not present in acidic media and the nucleophilic attack is conducted by a less nucleophilic water molecule adsorbing on the carbide surface. The thus formed TM–OH_2 single bond is weaker than a TM–OH bond (10 vs 500–600 kJ mol^{-1}).[53,54] In that case, the left term including $H_{C\text{-}TM}$ dominates Eq. 13. A simplification of Eq. 13 leads to the linear equation

$$H_{C-TM} * f + y = \eta_{Ox} \quad [14]$$

with empirical factors y and f describing the dependency of the overpotential on the transition metal—carbide bond strength. As the TM–OH_2 bond energy is more than one order of magnitude lower than $H_{C\text{-}TM}$, the variations in TM–OH_2 bond energy for different TMs can be neglected and y can be considered constant. If the rupture of the TM–C bond is the rds, Eq. 14 can be fitted to experimental results as shown in Fig. 4. If other electrolytes than 0.1 M $HClO_4$, or other H^+ concentrations than 10^{-1} M are used, it is suggested to probe the rds by determining η_{Ox} for at least 3 different TMCs. Additionally, the TM–O bond enthalpy becomes more significant for lower bond enthalpies which can result in a non-linear behavior.

Interpolation of E_{Ox} for other transition metal carbides.—If all before mentioned factors are considered, η_{Ox} can be interpolated from Eq. 14 for TMCs with $H_{C\text{-}TM}$ values in between the experimental determined boundaries. This was done for not experimentally investigated TMCs such as Sc_2C, Y_2C, La_2C, ZrC, HfC, Cr_3C_2 and Mo_2C (Fig. 4) because their $H_{C\text{-}TM}$ is in between the values of WC and TiC (Table SIII). By addition of η_{Ox} to E_{TMC}, the apparent

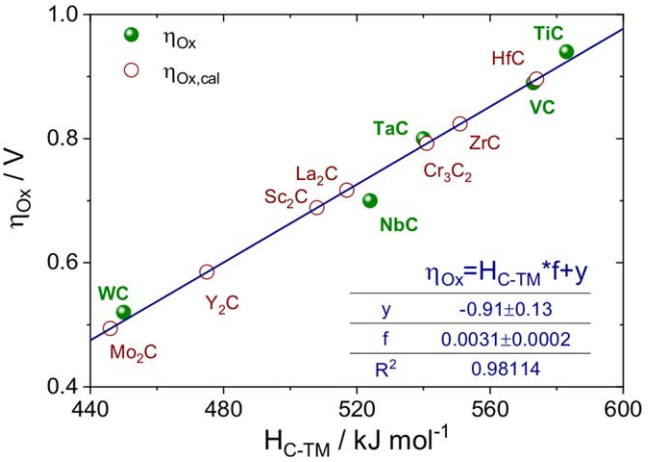

Figure 4. Overpotential as a function of the transition metal-carbon bond enthalpy ($H_{C\text{-}TM}$) for the measured TMCs and calculated values for other early TMCs according to the fitting parameters. Bond enthalpies taken from Ref. 41.

oxidation potentials E_{ox}^{cal} can be calculated (Fig. 5). As ZrC and HfC are also isomorph to NaCl with a 1:1 stoichiometry, the model seems reliably applicable. Compared to TiC, the calculated E_{ox}^{cal} are about 0.4 to 0.5 V lower despite a similar value for η, because of the high oxide formation enthalpy. The oxidation potential of ZrC is lower compared to the value reported by Kimmel et al. due to the presence of a ZrO_2 passivation layer.[14,28] Although not isomorph to NaCl, the model should also be applicable for metal carbides in the 3rd group as the TM sublattice has a fcc structure with half of the octahedral sites occupied by a C atom. Their E_{ox}^{cal} values are at least 0.22 V below RHE which is in accordance to previous reports describing their spontaneous decomposition upon contact with water.[6] Last, the E_{ox}^{cal} values of Cr_3C_2 and Mo_2C were calculated. The structure of both carbides is not fcc, hence, the calculated values of 0.58 V_{RHE} and 0.47 V_{RHE} for Cr_3C_2 and Mo_2C, respectively, have to be considered with care. Nonetheless, the experimentally determined value of Weidman et al. for Mo_2C fits well to the here calculated E_{ox}^{cal} suggesting that the model applies also for Cr_3C_2.[55] The reason might lie in the low energetical difference between the different carbide structures as for instance for hcp and fcc WC.[56] The here presented results demonstrate how the covalent character in metal carbides leads to an increased stability which might be adapted to other materials with certain shares of covalent bonding such as phosphides, sulfides, nitrides or borides.

Consequences for the usage of TMCs in electrocatalysis.—The model allows for the preselection of TMCs for electrochemical reactions by estimating the apparent oxidation potentials of various TMCs in acidic environment. Stability boundary conditions for the usage as support, protective coating or catalysts can be identified and compared to various electrochemical reactions. One example is the oxygen reduction reaction (ORR) in fuel cells where potentials above 1.0 V_{RHE} can occur.[57] As TiC, the TMC with the highest η_{Ox} and highest E_{Ox}, oxidizes at these potentials, none of the here investigated TMCs is immune at potentials over 1.0 V_{RHE} and a usage as support or catalyst is rather questionable. Besides the ORR, other electrochemical reactions such as the hydrogen evolution reaction (HER), the CO_2 reduction reaction (CO2RR) or the nitrogen reduction reaction (NRR) are more and more discussed in literature. For these reactions, lower potentials arise and TMCs are considered as catalyst or support. For the HER, WC has been tested as possible catalyst with high stabilities under reaction conditions.[10,13,25,58] However, according to DFT studies, electron donating TMCs like Sc_2C, Y_2C or HfC should be more active for reduction reactions.[7] According to the proposed model, it is suggested that they are stable as long as the potential is held below the oxidation potential as for example for Sc_2C below −0.36 V_{RHE}. A second possible application for the less noble carbides is the CO2RR which requires significantly lower potentials and all of the here investigated carbides are believed to be stable at CO2RR relevant potentials.[7,59] Similarly to the HER, WC has been investigated for the methanol oxidation reaction,[9,25] which starts usually around 0.5 V_{RHE}. Above this potential, WC is intrinsically unstable, but TiC, VC and NbC might be justifiable alternatives being immune against oxidation.[8]

Conclusion

In conclusion, the electrochemical stability of transition metal carbides was evaluated under acidic conditions and an oxidation model based on the metal-carbon bond strength was proposed. The model was experimentally derived by a detailed corrosion study of hexagonal tungsten carbide. For various refractory transition metal carbides, a linear dependency of the kinetic overpotential for the electrochemical oxidation on the transition metal—carbon bond enthalpy was observed in acidic media. The model allows for the estimation of apparent oxidation potentials for various early transition metal carbides and the correlation to experimental data. According to the model, the surface of transition metal carbides oxidizes under oxygen reduction relevant conditions, while they might be considered as potential catalyst or support for other electrochemical reactions. The presented model can be used for the estimation of stability windows of the transition metal carbide's

E_{TMC} / E_{ox}^{exp}	TMC	η_{Ox}^{cal} / E_{ox}^{cal}							
-1.05	Sc_2C	0.69	-0.09	TiC	0.92	-0.04	VC	0.89	-0.20	Cr_3C_2	0.79
		-0.36	0.85		0.84	0.85		0.85			0.59
-1.07	Y_2C	0.59	-0.41	ZrC	0.82	0.04	NbC	0.74	-0.02	Mo_2C	0.49
		-0.48			0.41	0.74		0.78			0.47
-0.94	La_2C	0.72	-0.40	HfC	0.90	-0.20	TaC	0.79	0.03	WC	0.51
		-0.22			0.49	0.60		0.59	0.55		0.53

Figure 5. Calculated thermodynamic oxidation potentials E_{TMC} at experimental conditions (upper left corner), calculated overpotential η_{Ox}^{cal} (upper right), observed oxidation potential E_{ox}^{exp} (blue, lower left) and calculated oxidation potential E_{ox}^{cal} (beige, lower right) of 3rd to 6th group transition metal carbides. Positions of the transition metal carbides reflect the position of the parent transition metal in the periodic table.

electrochemical surface for various electrochemical applications such as the hydrogen evolution, CO_2 reduction, or the methanol oxidation.

Acknowledgments

D.G., M.L. and K.J.J.M. thank the Federal Ministry for Economic Affairs and Energy (BMWi) of Germany in the framework of PtTM@HGS (project number 03ET6080A) for funding. M. P. thanks the International Max Planck Research School for Interface Controlled Materials for Energy Conversion (IMPRS-SurMat) for a scholarship. H.R. and J.M.S. gratefully acknowledge financial support from the MPG fellow program. Andrea Mingers is thanked for support and help with the ICP-MS.

References

1. S. T. Oyama, in *The Chemistry of Transition Metal Carbides and Nitrides*, ed. S. T. Oyama (Blackie Academic and Professional, Glasgow, UK) 1st ed. p 565 (1996).
2. Y. Xiao, J. Y. Hwang, and Y. K. Sun, *J. Mater. Chem. A*, **4**, 10379 (2016).
3. M. Messner, D. J. Walczyk, B. G. Palazzo, Z. A. Norris, G. Taylor, J. Carroll, T. X. Pham, J. D. Hettinger, and L. Yu, *J. Electrochem. Soc.*, **165**, H3107 (2018).
4. R. J. Colton, J.-T. J. Huang, and J. W. Rabalais, *Chem. Phys. Lett.*, **34**, 337 (1975).
5. H. H. Hwu and J. G. Chen, *Chem. Rev.*, **105**, 185 (2005).
6. T. Y. Kosolapova, in *Carbides—Properties, Production, and Applications* (Plenum Press, New York, USA) 1st ed. p 311 (1971).
7. M. G. Quesne, A. Roldan, N. H. De Leeuw, and C. R. A. Catlow, *Phys. Chem. Chem. Phys.*, **20**, 6905 (2018).
8. M. Roca-Ayats, G. García, J. L. Galante, M. A. Peña, and M. V. Martínez-Huerta, *J. Phys. Chem. C*, **117**, 20769 (2013).
9. G. Kawamura, H. Okamoto, A. Ishikawa, and T. Kudo, *J. Electrochem. Soc.*, **134**, 1653 (1987).
10. S. T. Hunt, T. M. Kokumai, D. Zanchet, and Y. Román-Leshkov, *J. Phys. Chem. C*, **119**, 13691 (2015).
11. R. D. Cowling and H. E. Hintermann, *J. Electrochem. Soc.*, **117**, 1447 (1970).
12. R. D. Cowling and H. E. Hintermann, *J. Electrochem. Soc.*, **118**, 1912 (1971).
13. F. Harnisch, G. Sievers, and U. Schröder, *Appl. Catal. B Environ.*, **89**, 455 (2009).
14. Y. C. Kimmel, X. Xu, W. Yu, X. Yang, and J. G. Chen, *ACS Catal.*, **4**, 1558 (2014).
15. C. H. Hendon, S. T. Hunt, M. Milina, K. T. Butler, A. Walsh, and Y. Román-Leshkov, *J. Phys. Chem. Lett.*, **7**, 4475 (2016).
16. S. T. Hunt, "Doctoral Thesis." Massachusetts Institute of Technology (2016).
17. A. Jablonski and J. Zemek, *Surf. Interface Anal.*, **41**, 193 (2009).
18. C. J. Powell and A. Jablonski, in *NIST Electron Inelastic-Mean-Free-Path Database, SRD 71, 1.2.* (National Institute of Standards and Technology, Gaithersburg MD) (2010).
19. E. McCafferty and J. P. Wightman, *Surf. Interface Anal.*, **26**, 549 (1998).
20. J.-P. Grote, A. R. Zeradjanin, S. Cherevko, and K. J. J. Mayrhofer, *Rev. Sci. Instrum.*, **85**, 104101 (2014).
21. R. J. Collins and H. Y. Fan, *Phys. Rev.*, **93**, 674 (1954).
22. K. Ogle, J. Baeyens, J. Swiatowska, and P. Volovitch, *Electrochim. Acta*, **54**, 5163 (2009).
23. D. Göhl, A. M. Mingers, S. Geiger, M. Schalenbach, S. Cherevko, J. Knossalla, D. Jalalpoor, F. Schüth, K. J. J. Mayrhofer, and M. Ledendecker, *Electrochim. Acta*, **270**, 70 (2018).
24. M. Wu, X. Lin, A. Hagfeldt, and T. Ma, *Angew. Chem. Int. Ed.*, **50**, 3520 (2011).
25. S. T. Hunt, T. Nimmanwudipong, and Y. Román-Leshkov, *Angew. Chem. Int. Ed.*, **53**, 5131 (2014).
26. K. M. Andersson and L. Bergström, *Int. J. Refract. Met. Hard Mater.*, **18**, 121 (2000).
27. M. C. Weidman, D. V. Esposito, I. J. Hsu, and J. G. Chen, *J. Electrochem. Soc.*, **157**, F179 (2010).
28. M. Pourbaix, in *Atlas of Electrochemical Equilibria in Aqueous Solutions* (NACE Interntional Ceelcor, Houston, Brussels) 1st ed. (1966).
29. Y. Li, G. Li, X. Wang, Z. Zhu, H. Ma, T. Zhang, and J. Jin, *Chem. Commun.*, **48**, 8222 (2012).
30. S. Yao, Y. Shimizu, N. Miura, and N. Yamazoe, *Chem. Lett.*, **19**, 2033 (1990).
31. M. W. J. Chase, in *NIST-JANAF Thermochemical Tables* (American Chemical Society, American Institute of Physics, National Institute of Standards and Technology, Gaithersburg, USA) 4th ed. (1998).
32. S. V. Meschel and O. J. Kleppa, *J. Alloys Compd.*, **205**, 165 (1994).
33. E. J. Huber, G. C. Fitzgibbon, E. L. Head, and C. E. Holley, *J. Phys. Chem.*, **67**, 1731 (1963).
34. L. Marsella and V. Fiorentini, *Phys. Rev. B-Condens. Matter Mater. Phys.*, **69**, 172103 (2004).
35. A. N. Kornilov, I. M. Ushakova, E. J. J. Huber, and C. E. J. Holley, *J. Chem. Thermodyn.*, **7**, 21 (1975).
36. G. K. Johnson, W. N. Hubbard, and E. K. Storms, *J. Chem. Thermodyn.*, **9**, 1021 (1977).
37. P. Hoffmann, H. Galindo, G. Zambrano, C. Rincón, and P. Prieto, *Mater. Charact.*, **50**, 255 (2003).
38. M. Krebsz, J. P. Kollender, and A. W. Hassel, *Phys. Status Solidi*, **214**, 1600803 (2017).
39. A. Abdulkadhim, T. Takahashi, D. Music, F. Munnik, and J. M. Schneider, *Acta Mater.*, **59**, 6168 (2011).
40. A. S. Kurlov and A. I. Gusev, *Inorg. Mater.*, **42**, 121 (2006).
41. J. Häglund, A. Fernández Guillermet, G. Grimvall, and M. Körling, *Phys. Rev. B*, **48**, 11685 (1993).
42. V. M. Cherkashenko, S. Z. Nazarova, A. I. Gusev, and A. L. Ivanovskii, *J. Struct. Chem.*, **42**, 1002 (2001).
43. S. T. Oyama, in *Kirk-Othmer Encyclopedia of Chemical Technology* (New York, Wiley) 4 (2015).
44. C. H. Hamann and W. Vielstich, in *Elektrochemie* (Wiley VCH Verlag GmbH, Weinheim, Germany) 4th ed. (2005).
45. R. F. Mann, J. C. Amphlett, B. A. Peppley, and C. P. Thurgood, *J. Power Sources*, **161**, 775 (2006).
46. W. Schmickler and E. Santos, in *Interfacial Electrochemistry* (Springer, Heidelberg, Germany) 2nd ed. (2010).
47. V. M. Schmidt, in *Elektrochemische Verfahrenstechnik* (Wiley VCH Verlag GmbH & Co. KGaA, Weinheim, Germany) 1st ed. (2003).
48. T. Kagiya, Y. Sumida, and T. Inoue, *Bull. Chem. Soc. Jpn.*, **42**, 2422 (1969).
49. G. Bartoli and P. E. Todesco, *Acc. Chem. Res.*, **10**, 125 (1977).
50. P. R. Wells, *Chem. Rev.*, **63**, 171 (1963).
51. S. Hu, K. Cheng, E. L. Ribeiro, K. Park, B. Khomami, and D. Mukherjee, *Catal. Sci. Technol.*, **7**, 2074 (2017).
52. J. G. Chen, *Surf. Sci. Rep.*, **30**, 1 (1997).
53. A. Michaelides, A. Alavi, and D. A. King, *Phys. Rev. B-Condens. Matter Mater. Phys.*, **69**, 113404 (2004).
54. M. F. Daniel, B. Desbat, J. C. Lassegues, B. Gerand, and M. Figlarz, *J. Solid State Chem.*, **67**, 235 (1987).
55. M. C. Weidman, D. V. Esposito, Y. C. Hsu, and J. G. Chen, *J. Power Sources*, **202**, 11 (2012).
56. A. H. Cottrell, *Mater. Sci. Technol.*, **11**, 209 (1995).
57. T. Mittermeier, A. Weiß, F. Hasché, and H. A. Gasteiger, *J. Electrochem. Soc.*, **165**, F1349 (2018).
58. M. Ledendecker, J. S. Mondschein, O. Kasian, S. Geiger, D. Göhl, M. Schalenbach, A. R. Zeradjanin, S. Cherevko, R. E. Schaak, and K. Mayrhofer, *Angew. Chemie Int. Ed.*, **56**, 9767 (2017).
59. S. K. Kim, Y. J. Zhang, H. Bergstrom, R. Michalsky, and A. Peterson, *ACS Catal.*, **6**, 2003 (2016).